Monthly Notices of the ROYAL ASTRONOMICAL SOCIETY

MNRAS **509,** 2856–2868 (2022) https://doi.org/10.1093/mnras/stab3203
Advance Access publication 2021 November 9

The 'breaking the chains' migration model for super-Earth formation: the effect of collisional fragmentation

Leandro Esteves [1]★ André Izidoro [1,2]★ Bertram Bitsch,[3] Seth A. Jacobson [4] Sean N. Raymond [5] Rogerio Deienno[6] and Othon C. Winter[1]

[1]*Grupo de Dinâmica Orbital e Planetologia, Universidade Estadual Paulista (UNESP), Guaratinguetá CEP 12516-410, SP, Brazil*
[2]*Department of Earth, Environmental and Planetary Sciences, MS 126, Rice University, Houston, TX 77005, USA*
[3]*Max-Planck-Institut für Astronomie, Königstuhl 17, D-69117 Heidelberg, Germany*
[4]*Department of Earth and Environmental Sciences, Michigan State University, East Lansing, MI 48824, USA*
[5]*Laboratoire d'astrophysique de Bordeaux, Univ. Bordeaux, CNRS, B18N, allée Geoffroy Saint-Hilaire, F-33615 Pessac, France*
[6]*Southwest Research Institute, 1050 Walnut St. Suite 300, Boulder, CO 80302, USA*

Accepted 2021 October 29. Received 2021 October 27; in original form 2021 September 14

ABSTRACT

Planets between 1 and 4 $R_\oplus$ (Earth radius) with orbital periods $<$100 d are strikingly common. The migration model proposes that super-Earths migrate inwards and pile up at the disc inner edge in chains of mean motion resonances. After gas disc dispersal, simulations show that super-Earth's gravitational interactions can naturally break their resonant configuration leading to a late phase of giant impacts. The instability phase is key to matching the orbital spacing of observed systems. Yet, most previous simulations have modelled collisions as perfect accretion events, ignoring fragmentation. In this work, we investigate the impact of imperfect accretion on the 'breaking the chains' scenario. We performed *N*-body simulations starting from distributions of planetary embryos and modelling the effects of pebble accretion and migration in the gas disc. Our simulations also follow the long-term dynamical evolution of super-Earths after the gas disc dissipation. We compared the results of simulations where collisions are treated as perfect merging events with those where imperfect accretion and fragmentation are allowed. We concluded that the perfect accretion is a suitable approximation in this regime, from a dynamical point of view. Although fragmentation events are common, only ∼10 per cent of the system mass is fragmented during a typical 'late instability phase', with fragments being mostly reacreted by surviving planets. This limited total mass in fragments proved to be insufficient to alter qualitatively the final system dynamical configuration – e.g. promote strong dynamical friction or residual migration – compared to simulations where fragmentation is neglected.

Key words: protoplanetary discs – planets and satellites: formation.

1 INTRODUCTION

Planets with sizes between those of Earth (1 $R_\oplus$) and Neptune (4 $R_\oplus$) – usually referred to as super-Earths (or mini-Neptunes) – are remarkably common around other stars. At least ∼30–50 per cent of the FGK spectral-type stars host super-Earths with orbital periods shorter than 100 d (Mayor et al. 2011; Howard et al. 2012; Fressin et al. 2013; Marcy et al. 2014; Mulders et al. 2018). Mercury – the innermost Solar system planet – has an orbital period of 88 d. Most observed super-Earths orbit their respective stars at orbits relatively closer than Mercury's orbit around the Sun. The high level of stellar irradiation that these planets receive from their parent stars has led these planets to be called 'hot' super-Earths (or hot mini-Neptunes). Given their apparent ordinariness and astonishing orbital configuration compared to Solar system planets, the origins of hot super-Earths are today an intense area of research. Models for the formation of hot super-Earths come in two flavours. In one school of thought, hot super-Earths are believed to have reached the innermost regions of the disc via gas-driven migration as they grow during the gas disc phase (e.g. Terquem & Papaloizou 2007; Ida & Lin 2008; Raymond, Barnes & Mandell 2008; Coleman & Nelson 2014; Cossou et al. 2014; Izidoro et al. 2017). In the second school of thought, super-Earths are believed to have formed '*in situ*' and without experiencing gas-driven radial migration (e.g. Raymond et al. 2008; Hansen 2014; Lee, Chiang & Ormel 2014; Ogihara, Morbidelli & Guillot 2015).

In this work, we model the formation of hot super-Earth systems in the context of the migration model. For a detailed discussion on why super-Earths are very unlikely to have completely avoided migration and formed '*in situ*', see Izidoro et al. (2021a).

The migration model for the origins of hot super-Earths proposes that super-Earth migrated inwards during the gas disc phase due to the planet–disc gravitational interactions (Terquem & Papaloizou 2007; Raymond et al. 2008; Ida & Lin 2010; McNeil & Nelson 2010). Super-Earths migrating inwards are not necessarily engulfed by the young star but most likely trapped at the gas disc inner edge (Masset et al. 2006; Romanova & Lovelace 2006; Flock et al. 2019). This dynamical evolution tends to produce long chains of planets locked in mean motion resonances anchored at the disc inner edge

★ E-mail: leandro.esteves@unesp.br (LE); izidoro.costa@gmail.com (AI)

(Ogihara & Ida 2009; Cossou et al. 2014; Izidoro et al. 2017, 2021a; Ogihara et al. 2018; Carrera, Ford & Izidoro 2019; Lambrechts et al. 2019). Planet–disc gravitational interaction effects damp planets' orbital inclinations and eccentricities (Cresswell & Nelson 2008; Bitsch & Kley 2010, 2011; Fendyke & Nelson 2014). As the gas disc dissipates, damping of orbital inclination and eccentricities becomes less efficient and eventually vanishes when the gas is fully dispersed. Numerical simulations show that the subsequent evolution of resonant chains bifurcates into two categories. In the first one, super-Earth systems remain dynamically stable preserving their pristine resonance state for billion of years (Esteves et al. 2020). In the second category, resonant chains become dynamically unstable – typically at the very end or just after the gas disc dispersal ($\lesssim$100 Myr). Late dynamical instabilities break resonances and lead to orbital crossing and giant impacts (Izidoro et al. 2017, 2021a). Systems that have experienced the late instability phase are typically referred to as 'unstable'. These planetary systems tend to be dynamically spread (non-resonant) with planets having relatively larger mutual orbital inclinations and eccentricities. On the contrary, 'stable' systems tend to have planets with very low eccentricity and inclination.

Numerical simulations show that the migration model matches fairly well the period ratio distribution of observed super-Earths when $\gtrsim$95–99 per cent of resonant chains become dynamically unstable (Izidoro et al. 2017, 2021a) and $\lesssim$5–1 per cent remain stable. We refer to this as the 'breaking the chains' (BTC) scenario. This model also predicts that most observed planetary systems showing single transit super-Earths are in fact multiplanet systems ($N \geq 2$). About $\sim$80 per cent of the observed stars hosting hot super-Earths show a single transiting planet, whereas only $\sim$20 per cent of the systems come with multiple transiting planets. This result is known as the *Kepler*'s dichotomy (Johansen et al. 2012). The BTC scenario suggests that the *Kepler*'s dichotomy is a consequence of observational bias (Izidoro et al. 2017, 2021a) and that most single transiting planets are not truly single. Simulated transit observations mixing a fraction of $<$5 per cent stable and $>$95 per cent unstable systems (fractions that produce a good match to the observed period ratio distribution of super-Earths) produce also a decent match to the *Kepler* planet multiplicity distribution and dichotomy (Izidoro et al. 2017, 2021a). The low mutual orbital inclination of planets in stable systems tends to favour the detection of multiple transiting planets if the observer is well aligned with the planets' ('common') orbital plane. Unstable systems, in contrast, tend to have planets with relatively larger mutual orbital inclinations that make them more likely to be missed by transit observations. This naturally enhances the number systems showing single transiting planets.

Although the BTC scenario provides an appealing framework to explain the origin of hot super-Earth system, it remains elusive how the simplistic treatment of impacts adopted in previous simulations influences the main results of the model. So far, all simulations in the context of the BTC scenario were performed modelling collisions as perfect merging events where mass and linear momentum are conserved (Izidoro et al. 2017, 2021a). Collisional fragmentation has been proposed to lead to self-destruction of hot super-Earth systems (Volk & Gladman 2015). This hypothesis seems to conflict with the results of numerical simulations showing successful planetary growth in regions as close as 0.04 au from the star (Wallace, Tremaine & Chambers 2017). One real possibility, however, is that fragments produced via impacts have the chance to interact with the final planets and extract them from mean motion resonances and/or damp their orbital eccentricity and inclinations (e.g. Chatterjee & Ford 2015). These effects could strongly alter the final dynamical architecture of planetary systems (e.g. masses, resonant configuration, number of planets, etc.) and how the migration model matches observations. The main goal of this paper is to revisit the BTC scenario using a more realistic treatment for impacts. We use *N*-body numerical simulations to model planetary growth via pebble accretion, gas-driven migration, and the long-term evolution of hot super-Earths. This work builds on previous studies (Bitsch et al. 2019; Lambrechts et al. 2019; Izidoro et al. 2021a). We compare the results of simulations where we model collisions using semi-analytical prescriptions calibrated from the output of hydrodynamical simulations (Leinhardt & Stewart 2012; Stewart & Leinhardt 2012) with the results of simulations where collisions are modelled as perfect merging events. We discuss the importance of considering imperfect accretion when modelling the formation of hot super-Earths.

This paper is structured as follows: In Section 2, we present our methods, the collision treatment algorithm, and simulation set-up. In Section 3, we show the results of representative simulations. In Section 4, we present a statistical analysis comparing the results of simulations where the effects of collisional fragmentation are accounted for and those where it is neglected. In Section 5, we discuss about the dust production and mantle-erosive collisions in our simulations. Finally, in Section 6 we discuss our model, results, and main conclusions.

2 METHODS

Our *N*-body simulations were performed using a new version of the MERCURY-FLINTSTONE code (Bitsch et al. 2019; Izidoro et al. 2021a). MERCURY-FLINTSTONE is a modified version of MERCURY *N*-body integrator package (Chambers 1999) that includes routines dedicated to model gas disc evolution, planet migration, gas tidal damping of inclination/eccentricity, gas-assisted pebble accretion, and gas accretion (for a detailed description of these routines, see Bitsch et al. 2019; Izidoro et al. 2021a). In this work, we have added a new feature to MERCURY-FLINTSTONE. We have upgraded the simplistic treatment of collisions used in the code – where collisions are always assumed to result in perfect merging events. We have implemented into our code a prescription to resolve collisions based on the outcome of impact hydrodynamical simulations (Leinhardt & Stewart 2012). Collisions in MERCURY-FLINTSTONE can now result in bouncing, fragmentation, and accretion. All our simulations were performed using the hybrid-sympletic integrator (Chambers 1999).

2.1 Collision model

MERCURY-FLINTSTONE uses the same algorithm of the regular MERCURY to identify collisions. At every time-step it checks if the distance between any two bodies is smaller than the sum of their physical radius. When this condition is matched, a collision is flagged to be resolved. One of the caveats of this approach is that a collision may be identified when colliding bodies have already largely overlapping physical radii. In this situation, to properly resolve the collision, we need to restore the dynamical state of the colliding bodies to the very moment when they 'touch' each other. We account for this issue by integrating the motion of the colliding bodies back in time. We use a three-body approximation (sun and colliding bodies) and the Bulirsch–Stoer integration algorithm with accuracy parameter set to 10^{-15}, which ensures a small time-step. We stop this reversal integration at the first time-step when the distance between the bodies becomes larger than their combined physical radius. We use the

dynamical state of colliding bodies at this specific instant to resolve the collisions as described below.

Following Leinhardt & Stewart (2012), we define the more massive body involved in a collision as 'target' (thereafter use the subscript t) while the less massive planetary body is referred to as 'projectile' (thereafter we use the subscript p). M_t and M_p represent the masses of the target and projectile, respectively. R_t and R_p are their respective physical radius. V_{imp} is their impact velocity, Q is the impact energy, b is the impact parameter given by $b = \sin(\theta)$, where θ is the impact angle. b_{crit} represents the critical impact parameter that sets the threshold between grazing ($b > b_{crit}$) and non-grazing ($b < b_{crit}$) collisions. M_{int} is the interacting total mass, Q'^{*}_{RD} is the critical impact energy, and $Q^{\dagger *}_{RD}$ is the critical impact energy of the reverse impact [we refer the reader to Leinhardt & Stewart (2012) for detailed description of these quantities].

Following Leinhardt & Stewart (2012), we express the outcome of a collision in terms of (i) the largest (most massive) remnant object; (ii) the second largest remnant object; and (iii) a population of relatively smaller fragments. We also classify impacts in different regimes: (i) perfect merge; (ii) supercatastrophic; (iii) partial erosion; (iv) partial accretion; (vi) erosive hit-and-run; (vii) graze-and-merge; and (viii) pure hit-and-run. For each impact category, we describe how we calculate the masses of the largest and second largest remnants, and respective smaller fragments. We refer to the largest and second largest remnant using the subscripts LR and SLR, respectively (e.g. M_{lr} is largest remnant mass). In our model, mass is always conserved when we resolve collisions, i.e. $M_t + M_p = M_{lr} + M_{slr} + M_{frag} = M_{tot}$, where M_{frag} represents the total mass in fragments. We start by describing impact regimes within the non-grazing category ($b < b_{crit}$).

(i) **Perfect merge regime:** If $V_{imp} < V_{\alpha,esc}$, where $V_{\alpha,esc}$ is the surface escape velocity of the interacting mass (M_{int}), given by

$$V_{\alpha,esc} = \sqrt{2GM_{int}/(R_t + R_p)}. \quad (1)$$

In the perfect merge regime, $M_{lr} = M_t + M_p$, $M_{slr} = 0$ and $M_{frag} = 0$.

(ii) **Supercatastrophic regime:** If $V_{imp} \geq V_{sc}$, where V_{sc} is the supercatastrophic critical velocity expressed in terms of the supercatastrophic disruption energy $Q_{sc} = 1.8Q'^{*}_{RD}$, collision combined mass $M_{tot} = M_t + M_p$ and reduced mass $\mu = M_t M_p/M_{tot}$, defined as

$$V_{sc} = \sqrt{2Q_{sc}M_{tot}/\mu}. \quad (2)$$

The supercatastrophic regime corresponds to the case where fragmentation takes place and the largest remnant receives less than 10 per cent of the impact combined mass. The mass of the largest remnant is calculated as

$$M_{lr} = 0.1M_{tot}\left(\frac{Q}{1.8Q'^{*}_{RD}}\right)^{-3/2}. \quad (3)$$

(iii) **Partial erosion regime:** If $V_{imp} \geq V_{ero}$, where V_{ero} is the erosive critical velocity expressed as

$$V_{ero} = \sqrt{2Q_{ero}M_{tot}/\mu}, \quad (4)$$

with the critical erosive energy set $Q_{ero} = Q'^{*}_{RD}\left(\frac{2M_p}{M_{tot}}\right)$. The mass of the largest remnant is given as

$$M_{lr} = M_{tot}\left(1 - \frac{Q}{2Q'^{*}_{RD}}\right). \quad (5)$$

(iv) **Partial accretion regime:** If $b < b_{crit}$ and $V_{imp} < V_{ero}$. The transition between the erosion and accretion regimes occurs when the largest remnant mass becomes smaller than the initial target mass. As in the previous regime,

$$M_{lr} = M_{tot}\left(1 - \frac{Q}{2Q'^{*}_{RD}}\right). \quad (6)$$

For grazing impacts ($b > b_{crit}$), the following regimes can be defined:

(v) **Supercatastrophic hit-and-run regime:** If $V_{imp} \geq V^{\dagger}_{sc}$, where $V^{\dagger}_{sc}$ is the supercatastrophic critical velocity of the reverse impact defined as

$$V^{\dagger}_{sc} = \sqrt{2Q^{\dagger}_{sc}M_{int}/\mu_{int}}. \quad (7)$$

μ_{int} is the interacting reduced mass. $Q^{\dagger}_{sc} = 1.8Q^{\dagger *}_{RD}$ defines the critical impact energy for an impact where the largest remnant from the projectile receives less than 10 per cent of the interacting total mass (M_{int}). In this case, $M_{lr} = M_t$ (fragmentation occurs only for the projectile).

(vi) **Erosive hit-and-run regime:** If $V_{imp} \geq V^{\dagger}_{ero}$, where $V^{\dagger}_{ero}$ is the erosive critical velocity of the reverse impact given by

$$V^{\dagger}_{ero} = \sqrt{2Q^{\dagger}_{ero}M_{int}/\mu}, \quad (8)$$

where the critical erosive impact energy is $Q^{\dagger}_{ero} = Q^{\dagger *}_{RD}\left(\frac{2M_{p,int}}{M_{int}}\right)$. $M_{p,int}$ is the projectile mass that effectively interacts with the target. In this case $M_{lr} = M_t$ and

$$M_{slr} = M_{int}\left(1 - \frac{Q^{\dagger}}{2Q^{\dagger *}_{RD}}\right). \quad (9)$$

The fragments total mass is $M_{frag} = M_{tot} - M_{lr} - M_{slr}$.

(vii) **Graze-and-merge regime:** If $V_{imp} < V_{hr}$, where V_{hr} is the threshold velocity defining the boundary between the hit-and-run and graze-and-merge regimes. Following Kokubo & Genda (2010), it is defined as

$$\frac{V_{hr}}{V_{esc}} = c_1\zeta^2(1-b)^{5/2} + c_2\zeta^2 + c_3(1-b)^{5/2} + c_4, \quad (10)$$

where $\zeta = (M_t - M_p)/M_{tot}$. All coefficients c_i are given in Genda, Kokubo & Ida (2012). V_{esc} is the surface escape velocity of the combined mass of the colliding bodies. As in the perfect merge regime, $M_{lr} = M_t + M_p$, $M_{slr} = 0$.

(viii) **Pure hit-and-run regime:** If $V_{imp} > V_{hr}$. In this case, the colliding bodies conserve their original masses.

We can now define the mass of the second largest remnant in regimes (ii), (iii), (iv), and (v). For these regimes, M_{slr} is calculated as Leinhardt & Stewart (2012) via the following equation:

$$M_{slr} = M_{tot}\frac{(3-\beta)\left(1 - N_{lr}\frac{M_{lr}}{M_{tot}}\right)}{N_{slr}\beta}, \quad (11)$$

where β is the power-law slope of the mass/size distribution of fragments obtained via fits to the results of hydrodynamical simulations. We assume $\beta = 2.85$, as suggested by Leinhardt & Stewart (2012). $N_{lr} = 1$ and $N_{slr} = 2$ are the integer indexes representing LR e SLR, respectively. C is a proportionality constant defined in Leinhardt & Stewart (2012). Once we have calculated M_{slr}, we can also compute the total mass in fragments as $M_{frag} = M_{tot} - M_{lr} - M_{slr}$.

We calculated the mass distribution of fragments following the prescription (fits) provided in Leinhardt & Stewart (2012). Due to computational limitations, we truncated the minimum fragment mass to M_{min}, to avoid an extremely large number fragments in our N-body simulations. After a series of test simulations, we found that $M_{min} = 10\ M_{Ceres}$ provides a good compromise between the typical number of fragments created and the CPU-time required to complete our

Table 1. Comparing the outcome of selected collisions in MERCURY-FLINTSTONE, LIPAD, and SYMBA. Each line represents one particular collision. From left to right, the columns show target mass, projectile mass, impact velocity normalized by the escape velocity, impact parameter, total mass in fragments produced by each code, and collisional regime following Leinhardt & Stewart (2012). The collisional algorithm included in LIPAD is based on the results from Benz & Asphaug (1999) and that from SYMBA is described in Chambers (2013). SYMBA and LIPAD follow slightly different terminologies to refer to some collisional regimes relative to those used in this paper. Note also that for each collision the quantities $V_{\rm imp}$ and b are calculated in MERCURY-FLINTSTONE when the bodies collide. These quantities may be slightly different from those calculated in LIPAD and SYMBA, because these codes use different numerical integrators and slightly different algorithms to find the very instant when the bodies 'touch' in a collision. This mostly accounts for the observed differences between the codes. The goal of this table is only to demonstrate that the codes agree qualitatively well in terms of the total fragmented mass produced in different collisional regimes.

$M_{\rm t}$	$M_{\rm p}$	$V_{\rm imp}$	b	Collisional regime	$M_{\rm frag}$ ($M_\oplus$)		
($M_\oplus$)	($M_\oplus$)	($V_{\alpha,{\rm esc}}$)			MERCURY-FLINTSTONE	LIPAD	SYMBA
3.7328	1.2850	1.1800	0.5787	Partial accretion	0.1218	0.0962	0.1218
2.3779	1.7084	1.8664	0.819	Pure HnR	0.0	0.2404	0.0
3.1019	0.5349	2.2078	0.9165	Erosive HnR	0.2169	0.1260	0.1702
5.7984	3.6118	4.2028	0.9428	Supercatastrophic HnR	2.8996	2.9518	2.2840
4.1616	2.1033	11.0729	0.4275	Supercatastrophic	6.2075	6.2647	6.2630
8.4263	4.0463	1.3960	0.7395	Graze-and-merge	0.0	0.4519	0.0
1.6815	1.0191	5.1664	0.509	Partial erosion	2.0510	1.2879	2.6999
					Total ($M_\oplus$)		
					11.4968	11.4189	11.5389

simulations. Each simulation performed here requires between 2000 and 5000 CPU-hours on a single processor of a Xeon E5-2630 v4 processor at 2.2 GHz.

The number of fragments with mass between $M_{\rm slr}$ and $M_{\rm min}$ is calculated as

$$N(M_{\rm slr}, M_{\rm min}) = \frac{C}{\beta 2^{\beta}} \left(M_{\rm min}^{-\frac{\beta}{3}} - M_{\rm slr}^{-\frac{\beta}{3}} \right) \left(\frac{4\pi\rho}{3} \right)^{\frac{\beta}{3}}, \quad (12)$$

where ρ represents the fragments' bulk density. The mass of the nth fragment is iteratively calculated via the following equation:

$$M_n = \frac{4\pi\rho}{3} \left(\frac{3(3-\beta)}{4\pi\rho C} M_{\rm rem} \right)^{3/(3-\beta)}, \quad (13)$$

where $M_{\rm rem}$ is the remaining mass in fragments after each iteration. When $M_n \leq M_{\rm min}$, the remaining mass in fragments is distributed to (one or more) equal mass fragments with mass set equal to $M_{\rm min}$. If at the very last iteration, $M_{\rm rem} \leq M_{\rm min}$, we add the remaining mass to the previous fragment (iteration $n-1$) to ensure mass conservation rather than creating a new fragment. Our algorithm yields linear momentum conservation in collisions within a margin of $\sim$5 per cent. For collisions where $M_{\rm frag} < M_{\rm min}$, the collision is transferred to the perfect merge or graze-and-merge regimes.

We resolve collisions by placing the LR at collision's centre of mass. The SLR and fragments are placed at equidistant positions from each other on a circumference located at the plane of the impact and centred at LR. The circumference radius corresponds to 1 hill radius of the total mass ($M_{\rm tot}$). We assume that this circumference can accommodate up to 500 fragments, in order to prevent fragments from having 'overlapping' starting positions. If more than 500 fragments are produced in a single collision we create another circumference with radius 10 per cent larger than the original one. We repeat this procedure until we can distribute all fragments around the body LR. We calculate the velocities of the LR, SLR, and fragments following Leinhardt & Stewart (2012). The collisional model implemented here does not take into account the possible pre-impact spin rates of colliding bodies. In a first approximation, the pre-impact spin may act reducing the disruption criteria (critical impact energy to lead to fragmentation), which may increase the fragmented mass. In our simulations, we assume that colliding bodies are not spinning.

We have compared our algorithm to solve collisions with those used in LIPAD (Levison, Duncan & Thommes 2012) and a modified version of SYMBA (Duncan, Levison & Lee 1998; Poon et al. 2020; Scora et al. 2020). We present these results in Table 1. Each line in Table 1 represents one collision event. From left to right, the columns show the masses of the target and projectile, impact velocity, impact parameter, total fragmented mass, and collisional regime. Table 1 shows that, for all collisions, the fragmented mass produced in MERCURY-FLINTSTONE agrees within a margin of <25 per cent (in most cases the difference is only a few per cent) with that of one of the two codes. In our model, the fragment population is distributed following the mass/size distribution and velocities predicted by the results of hydrodynamical simulations (Leinhardt & Stewart 2012). Poon et al. (2020) and Scora et al. (2020) follow Chambers (2013), and assume that the fragment population consist of equal mass/size objects. In LIPAD, fragments are distributed following the algorithms described in Benz & Asphaug (1999) and Morbidelli et al. (2009). Although these codes invoke slightly different prescriptions for the distribution of fragments, we will discuss later that our results support qualitatively the main conclusions from previous studies using SYMBA and LIPAD, and applied in different contexts.

3 SIMULATIONS

We have performed 100 N-body numerical simulations modelling the formation of super-Earths considering the effects of pebble accretion and planet–disc gravitational interactions. Our simulations come in two groups. The first group consists of 50 simulations where we neglect the effects of collisional fragmentation, i.e. collisions always result in perfect accretion and linear momentum conservation. We refer to this group of simulations as 'perfect set'. The second group consists of 50 simulations where collisions may also result in imperfect accretion, as described before. We refer to this group as 'imperfect set'. The prescriptions of type-I migration, gas tidal

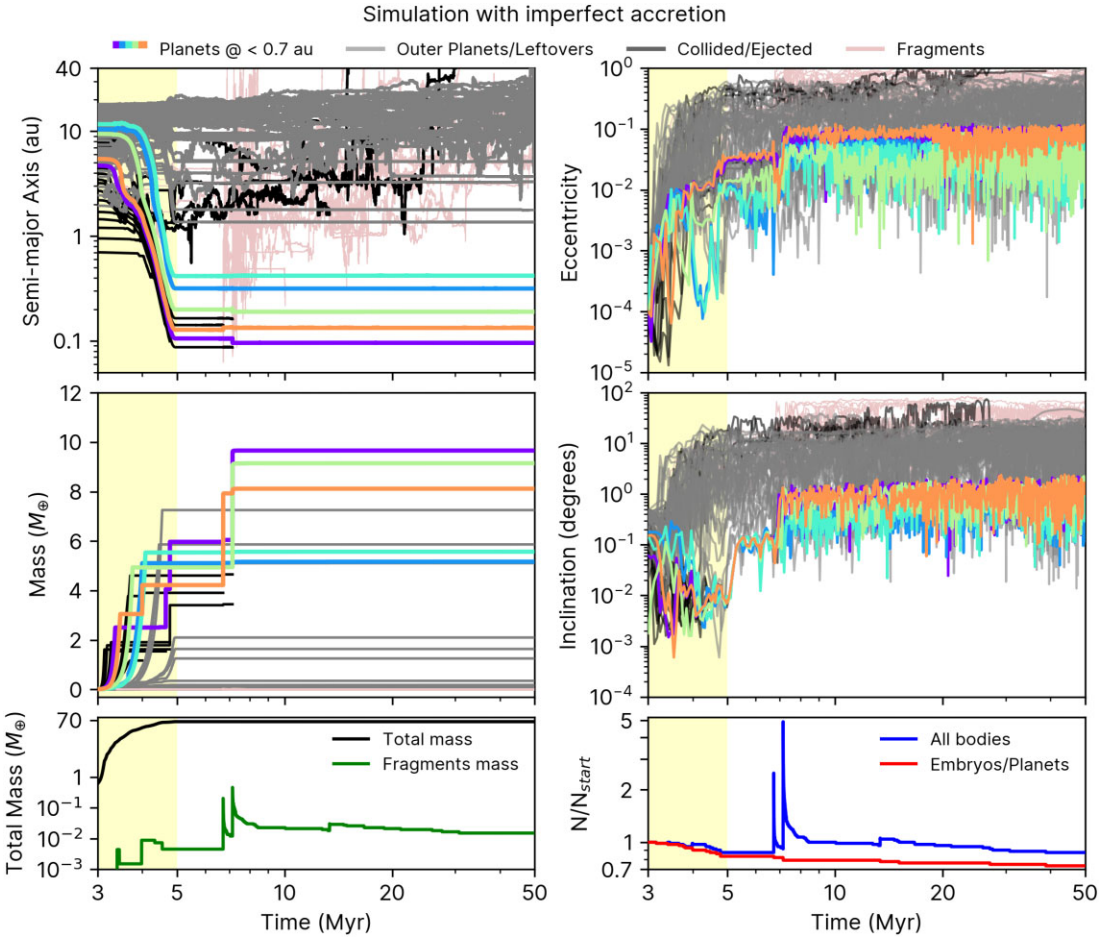

Figure 1. Growth and dynamical evolution of planetary embryos in a simulation where collisions may result in imperfect accretion. The light yellow background marks the gas disc phase. Colourful lines illustrate the planets with final orbits inside 0.7 au. The grey lines show the planets or embryos leftovers with final orbits outside 0.7 au. Black lines denote collided/ejected planets/embryos. The light red lines show fragments produced in collisions. *Top left*: Temporal evolution of semimajor axis. *Top right*: Evolution of orbital eccentricity. *Middle left*: Temporal evolution of planetary mass. *Middle right*: Evolution of orbital inclination. *Bottom left*: Evolution of the total system mass (black line) and total fragment mass (green line). *Bottom right*: The blue line shows the total number of bodies in simulation and red line shows the number of embryos/planets only. These numbers are normalized by the initial number of bodies in the simulation.

damping, pebble drift, pebble accretion, and gas disc models invoked in this paper are detailed described in Lambrechts et al. (2019) and Izidoro et al. (2021a).

Our numerical simulations start from initial conditions equivalent to those of Model-I of Izidoro et al. (2021a). We have chosen this model in light of its success in matching the period ratio distribution of observations. Protoplanetary embryos are initially distributed between 0.7 and 20 au with masses randomly selected between 0.005 and 0.015 $M_\oplus$. Our simulations start when the gas disc is 3 Myr old (t_{start} = 3 Myr). Protoplanetary embryos are allowed to grow via accretion of drifting pebbles and collisions. The integrated pebble flux in our simulations – from 3 to 5 Myr – yields ∼150 $M_\oplus$ in pebbles. The final masses of planets growing in simulations modelling pebble accretion strongly depend on the available pebble flux (Bitsch et al. 2019; Lambrechts et al. 2019; Izidoro et al. 2021a). If the integrated pebble flux is very low (e.g. ∼40 $M_\oplus$), planetary embryos tend to grow at most to Moon/Mars-mass planets (Lambrechts et al. 2019; Izidoro, Bitsch & Dasgupta 2021b) whereas a very high pebble flux (e.g. ∼300 $M_\oplus$) tend to produce gas giant planets (Bitsch et al. 2019). The pebble flux chosen to conduct our simulations is intentionally designed to produce super-Earth mass planets as shown by Izidoro et al. (2021a). The gas disc dissipates at 5 Myr and we extend our simulations up to 50 Myr in a gas-free scenario. We do not model gas accretion on to planetary embryos in our simulations. Our super-Earths are assumed to have a bulk density of 2 g cm^{-3}. This same density is used to compute the critical Q'^{*}_{RD} in our collisional algorithm.

We do not directly compare the results of our simulations with observations in this paper. This analysis is conducted in Izidoro et al. (2021a). We show, however, that the results of this paper support the main findings and conclusions of Izidoro et al. (2021a). In the next section, we show the dynamical evolution of growing planets in two representative simulations of the perfect and imperfect sets.

3.1 Dynamical evolution

Fig. 1 shows the dynamical evolution of growing planets in a simulation of the imperfect set. This simulation starts with 71 protoplanetary embryos carrying an initial total mass of 0.6 $M_\oplus$ (bottom panel of Fig. 1). During the gas disc phase planets grow by pebble accretion and collisions. As they grow to sufficiently large masses ($\gtrsim$0.1 $M_\oplus$) they start to migrate (top-left panel of Fig. 1). More massive protoplanetary embryos scatter less massive ones on eccentric and inclined orbits (grey and black curves in the top-

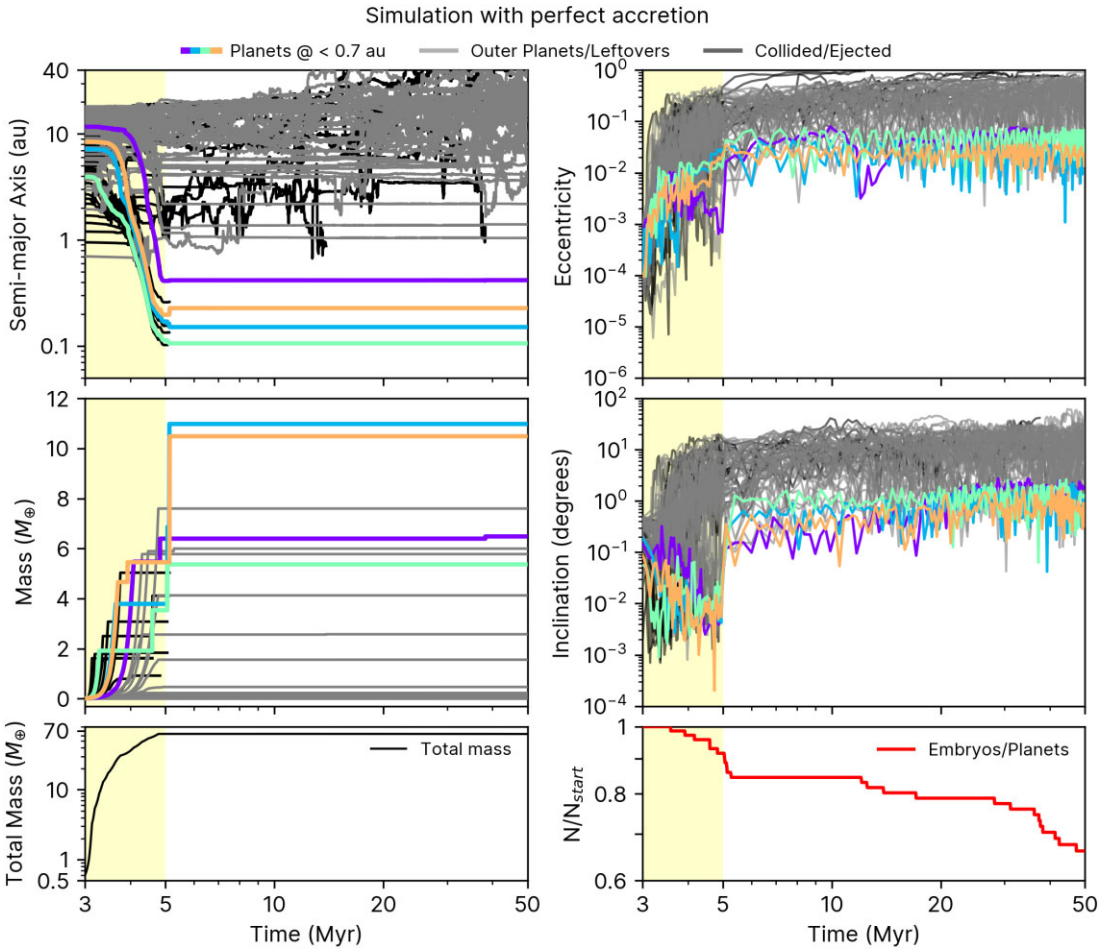

Figure 2. Same as Fig. 1, but for a simulation modelling collisions using the perfect accretion approach.

right and middle-right panels of Fig. 1). Collisions during the gas disc phase also lead to fragmentation (bottom-left panel of Fig. 1), although to some limited degree. At the end of the gas disc phase a chain of planets anchored at the disc inner edge set at 0.1 au forms (top-left panel of Fig. 1), with the most massive protoplanets having masses between 1 and 7 $M_\oplus$ (middle-left panel of Fig. 1). At the end of the gas disc phase the total mass carried by protoplanets is about ∼63 $M_\oplus$. After the gas disc dispersal the resonant chain becomes dynamically unstable, at 7 Myr. The dynamical instability promote collisions and fragmentation. Fragments that survive for more than 1000 yr after their creation are shown via light red lines in Fig. 1. The planet represented by the orange line is the outcome of a partial accretion collision occurred during the instability phase. In this particular event 275 fragments were produced. The planet represented by the purple line is also result of a grazing and merge collision during the instability phase. The green line shows a planet produced in a partial accretion where 582 fragments were produced. The total mass in fragments produced during the instability phase is about 0.64 $M_\oplus$. Fragments produced during impacts tend to be rapidly accreted and scattered by protoplanets as shown by the bottom panels of Fig. 1. At the end of the simulation, five planets survive inside 0.7 au with masses between 4 and 10 $M_\oplus$.

Fig. 2 shows the dynamical evolution of protoplanets in a simulation of perfect accretion set. This simulation starts from the same set of initial conditions (same mass and orbital elements for all protoplanets) and set-up of that of Fig. 1. Although the overall dynamical evolution of the system in Fig. 1 is similar to that of Fig. 2, the chaotic nature of planet formation simulations prevent us from directly comparing individual systems. In order to effectively measure the effects of imperfect accretion on the BTC scenario, we need to invoke a statistical analysis. Note also that Figs 1 and 2 represent systems where the resonant chains become dynamically unstable after the gas disc dispersal (the 'unstable' systems of Izidoro et al. 2021a). We will discuss the fraction of unstable and stable systems in our simulations in Section 4.

4 STATISTICAL ANALYSIS

In this section, we compare the dynamical architecture of planetary systems produced in our imperfect and perfect accretion sets of simulations using a statistical approach. In order to infer the role of fragmentation during and after the gas disc dispersal, we divide our analysis in two steps. We first compare the imperfect and perfect set of simulations using the dynamical architecture of planetary systems produced at the end of the gas disc phase (5 Myr). Finally, we repeat this analysis comparing their dynamical state at the end of our simulations. We use the period ratio of adjacent planet pairs, planets mutual spacing, orbital eccentricity, orbital inclination, mass, and planet multiplicity distributions as metrics to discuss our results.

4.1 Dynamical architecture at the end of the gas disc phase

Following Izidoro et al. (2021a), we apply cut-offs in our data when conducting our statistical analysis. As we are particularly interested

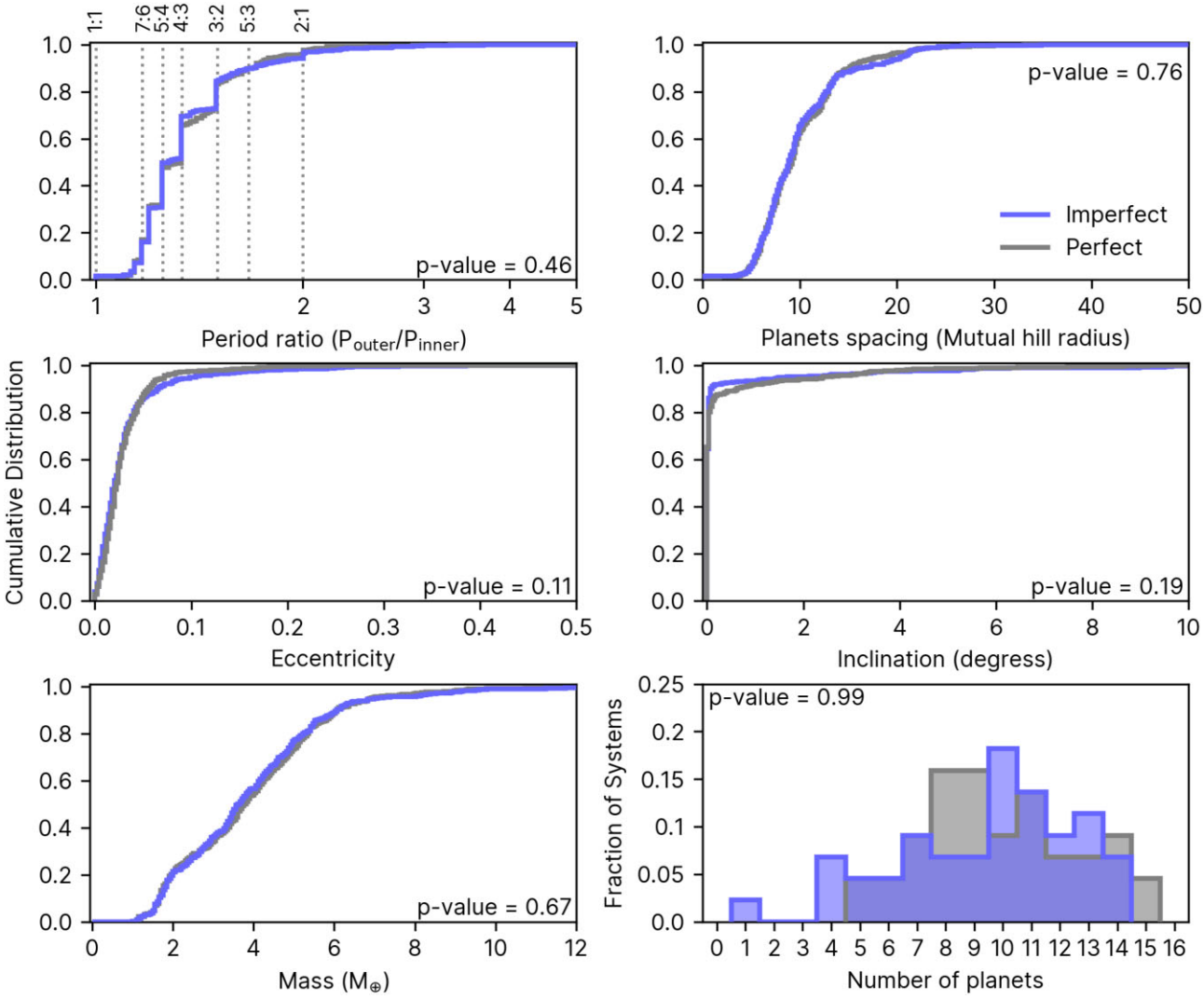

Figure 3. Dynamical architecture of planetary systems at the end of gas disc phase for planets/embryos that ended within 0.7 au with masses greater than 1 $M_\oplus$. Blue lines denote imperfect accretion set simulations and grey lines represent the simulations from perfect accretion set. Each panel also shows the *p*-value from K–S tests comparing the respective distributions of the imperfect and perfect sets. *Top left*: Cumulative distribution for the period ratio between adjacent planet pairs. Vertical dotted lines illustrate ratios values for possible first-order mean motion resonances and co-orbital planet pairs. *Top right*: Spacing between planet pairs given in terms of the mutual hill radius. *Middle left/right*: Cumulative distribution for planets orbital eccentricity/inclination. *Bottom left*: Cumulative distribution for planetary mass. *Bottom right*: Multiplicity of planets in systems versus the fraction of simulations from imperfect and perfect sets. In some systems, the onset of dynamical instability phase takes place just before the end of the gas disc phase, typically during the last few ∼100 Kyr. We have verified that these same distributions at 4.75 Myr are only slightly different from those at 5 Myr. More importantly, the K–S tests for all distributions still support our conclusions that the distributions of the perfect and imperfect sets are statistically the same.

in the formation of hot super-Earths, only planets more massive than 1 $M_\oplus$ and inside 0.7 au are accounted for in our analysis. These cut-offs are motivated by the high completeness of the *Kepler* catalogue for planets larger than the Earth and with orbital period shorter than 200 d (Petigura, Marcy & Howard 2013) (for a solar-mass star, a planet at 0.7 au has orbital period of about 200 d). All the same, we have verified that our results do not change qualitatively when we relax these thresholds and include all planets inside 2 au and with masses larger than 0.5 $M_\oplus$.

Fig. 3 shows the period ratio of adjacent planet pairs, planets spacing, orbital eccentricity, orbital inclination, mass, and number of planets distributions in our simulations at the end of the gas disc phase (5 Myr). In agreement with previous studies (Izidoro et al. 2017; Ogihara et al. 2018; Carrera et al. 2019), at the end of the gas disc phase planets are found in chain of mean motion resonances (top-left panel of Fig. 3) and in low-eccentricity and inclination orbits (middle panels of Fig. 3). More than 50 per cent of the planets formed in these simulations have masses between 2 and 6 $M_\oplus$. Both imperfect and perfect sets of simulations show remarkably similar distributions. We have used K–S tests to compare the respective distributions of the imperfect and perfect sets of simulations shown in Fig. 3. The respective *p*-values are shown inside each panel. By assuming that a *p*-value larger than 10 per cent implies that we cannot reject the null hypothesis that both set are drawn from the same distribution, we conclude that the imperfect and perfect set of simulations lead to statistically indistinguishable results.

In the next section, we show the impact velocity and geometry of collisions in our simulations and quantify the fraction of collisions falling in each collisional regime.

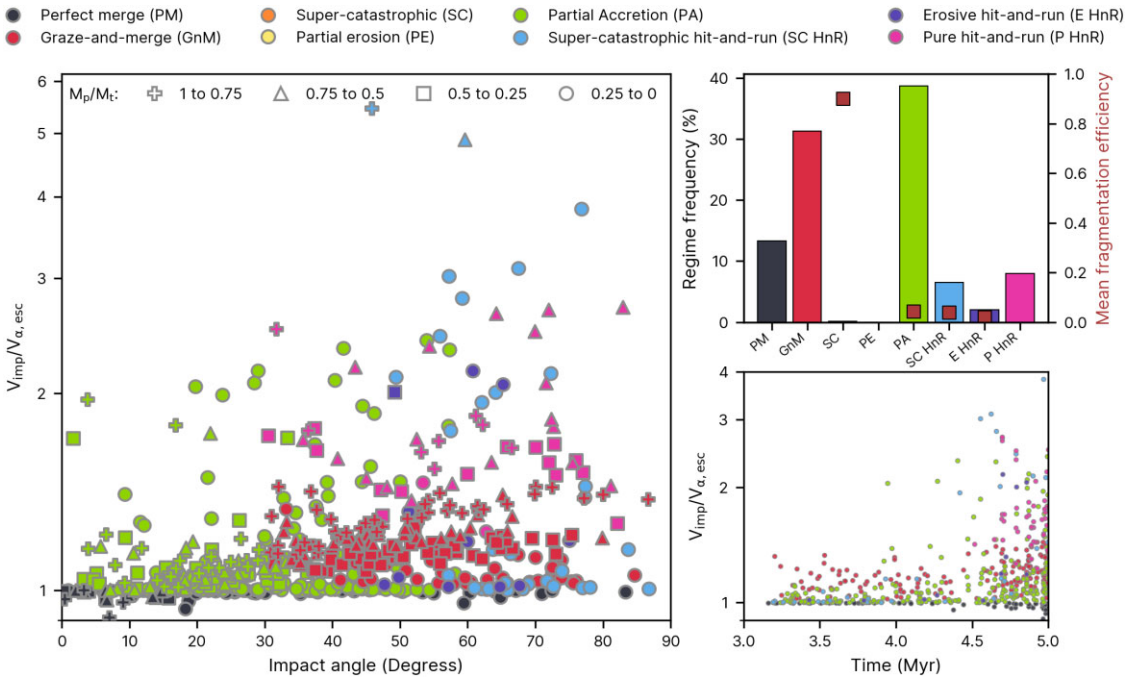

Figure 4. *Left-hand panel*: Impact geometry and velocity in collisions taking place during the gas disc phase in the imperfect set of simulations. Colour-coded symbols represent different collisional regimes. Each symbol shape denotes a mass ratio interval for the collision. The impact velocity is normalized by the surface escape velocity of the interacting total mass. *Top-right panel* shows the frequency (bars plot) and mean fragmentation efficiency (squares plot) of each regime. *Bottom-right panel* shows the impact velocities sa a function of time.

4.2 Collisions during the gas disc phase

Fig. 4 shows all collisions that occurred during the gas disc phase in the imperfect set of simulations. Colour-coding is used to show their respective regime as described in Section 2. The left-hand panel shows the impact geometry of all collisions. The top-right panel of Fig. 4 shows the frequency and fragmentation efficiency of each regime. Perfect merge and graze-and-merge regimes correspond to about 44.5 per cent of all collisions taking place during the gas disc phase. About 40 per cent of the collisions fall into the partial accretion regime. About 16 per cent of the cases are erosive, pure, and super-catastrophic hit-and-run impacts. Although the fraction of collisions in the partial-accretion regime is considerably high the top-right panel of Fig. 4 shows that, on average, the total mass in fragments produced in these collisions corresponds to a few per cent of the total colliding mass. This is also true for collisions in the supercatastrophic and erosive hit-and-run. One of the most energetic collisions observed in our simulations occurred between two Mercury-mass fragments (by-products of an anterior collision) that collided at velocities of $\sim$17 $V_{\alpha,\mathrm{esc}}$. In this particular case, a supercatastrophic collision occurred with more than 90 per cent of the colliding mass being fragmented. Note, however, that supercatastrophic and partial erosion collisions are extremely rare.

We have found that only 5 per cent of all collisions takes place at impact velocities higher than 2 $V_{\alpha,\mathrm{esc}}$. This is not a surprising result given that the gas helps to damp the orbital eccentricities and inclination of planetary embryos during the gas disc phase. In fact, the bottom-right panel of Fig. 4 shows that collisions taking place early in the disc phase tend to show lower impact velocities than those happening later. The reason for this is twofold. The impact velocity scales with the surface escape speed of the colliding bodies and their respective random velocities (their velocities before they become bounded). During the early stages of the disc, planetary embryos are less massive so their escape velocities are lower. During the early stages, the gas disc is also more dense, and damping of orbital inclination and eccentricity is more efficient. As the disc dissipates and bodies become more massive their impact velocities tend to increase, yet not up to the point where the effects of imperfect accretion becomes sufficiently important.

We have found that most fragments created during the gas disc phase have masses smaller than Moon mass. Fragments more massive than the Moon are only produced when the gas disc is almost fully dissipated and, consequently, they have virtually no time to accrete pebbles and grow via pebble accretion. In our model, we neglect pebble accretion on to fragments with masses lower than Moon mass (e.g. Johansen & Lambrechts 2017). We have verified that $\sim$70 per cent of the fragments created during the gas disc phase are quickly reacreted by larger protoplanetary embryos in time-scales of $\leq$50 kyr, so even if accounted for, they would have not time to grow significantly via pebble accretion. Fragments that survive longer time-scales have typically eccentric/inclined orbits so pebble accretion on these fragments would be also negligible (e.g. Levison, Kretke & Duncan 2015; Johansen & Lambrechts 2017). As fragments produced during the early disc phase are generally too small to accrete pebbles (or dynamically too hot) and fragments produced during the late disc phase do not have enough time to accrete significant mass in pebbles before the gas dissipates, fragments do not significantly increase the final mass of the planetary system compared to the perfect case (e.g. bottom-left panels of Figs 1 and 2). If pebble accretion on fragments was efficient, one could expect to have either a larger number of (potentially Earth-mass) planets in the system or more massive planets in the imperfect accretion case compared to the perfect case, which is clearly also not the case in Fig. 3. We can conclude that during the gas disc phase imperfect accretion have a negligible effect on the final dynamical architecture of super-Earth

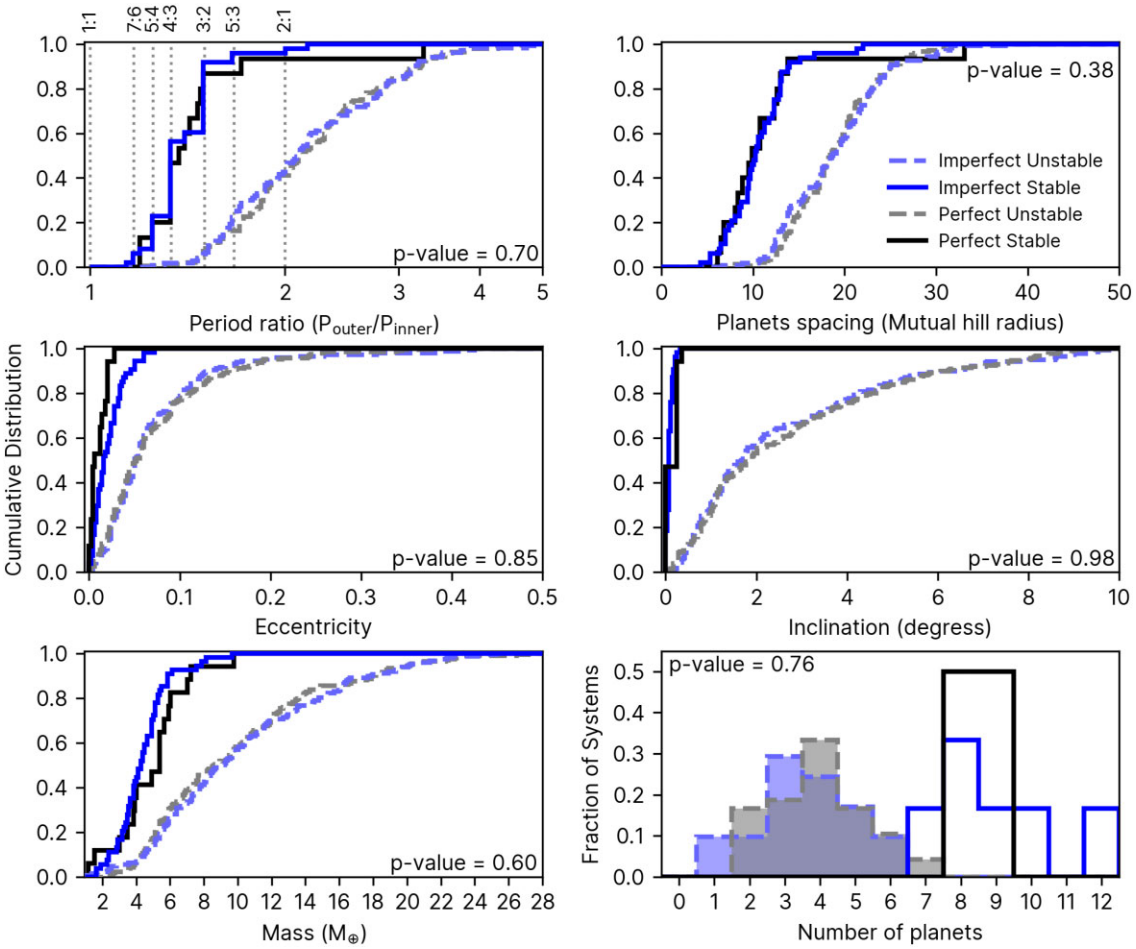

Figure 5. Final architecture of *unstable* (dashed lines) and *stable* (solid lines) planetary systems at 50 Myr. Panels show the *p*-value from K–S tests comparing the distributions from *unstable* systems of imperfect and perfect sets. Only planets/embryos with semimajor axis smaller than 0.7 au and masses greater than 1 $M_\oplus$ are taken into account. Blue colours and grey-scale colours illustrate the simulations from imperfect and perfect accretion sets, respectively. Panels are the same as those in Fig. 3.

systems forming via pebble accretion and migration due to the limited effect of fragmentation.

4.3 Final dynamical architecture

In this section, we compare the dynamical architecture of planetary system in the perfect and imperfect sets of simulations at the end of our simulations, namely at 50 Myr. We have found that ∼10 per cent of the resonant chains produced in the imperfect set remained dynamically stable until the end of our simulations, at 50 Myr. 4 per cent of the resonant chains of the perfect set remained stable. Due to the small number of 'stable' systems, we cannot firmly conclude that the difference in the fraction of 'stable' systems between the two sets is statically significant. A larger set of simulations would be desirable to provide a statically more robust conclusion. However, the low fraction of stable systems in these simulations is qualitatively consistent with the results of Izidoro et al. (2021a).

Following Izidoro et al. (2017, 2021a), we divided our planetary systems in two categories, the *unstable* and *stable* systems. Fig. 5 shows the orbital architecture of *unstable* and *stable* planetary systems of the perfect and imperfect sets of simulations after 50 Myr of integration. As for Fig. 3, Fig. 5 shows the period ratio, planet mutual spacing, orbital eccentricity, orbital inclination, mass, and number of planets distributions. Fig. 5 shows that – similar to what we have found at the end of the gas disc phase – the overall dynamical architecture of planetary systems in the perfect and imperfect sets of simulations are remarkably similar. As expected, planets in *stable* systems tend to have compact and resonant orbits whereas unstable system have more spread and dynamically excited orbits. Fig. 5 also shows in each panel the *p*-values calculated from K–S tests when we compare the respective distributions of our imperfect and perfect set of simulations. We do not apply K–S tests to compare stable systems due to the limited number of stable system in the sample. As one can see in all panels of Fig. 5, the distributions of stable systems in the perfect and imperfect sets do show some differences, but these are mostly due to small number statistics. The *p*-values calculated from our K–S tests confirm that the distributions of unstable systems at the end of simulations are statistically the same in the perfect and imperfect sets.

4.4 Collisions after the gas disc phase

Fig. 6 shows all collisions that occurred after the gas disc phase in the imperfect set of simulations. As in Fig. 4, colour-coding is used to represent different regimes. The left-hand panel shows the geometry of collisions. The top-right panel of Fig. 6 shows the frequency and

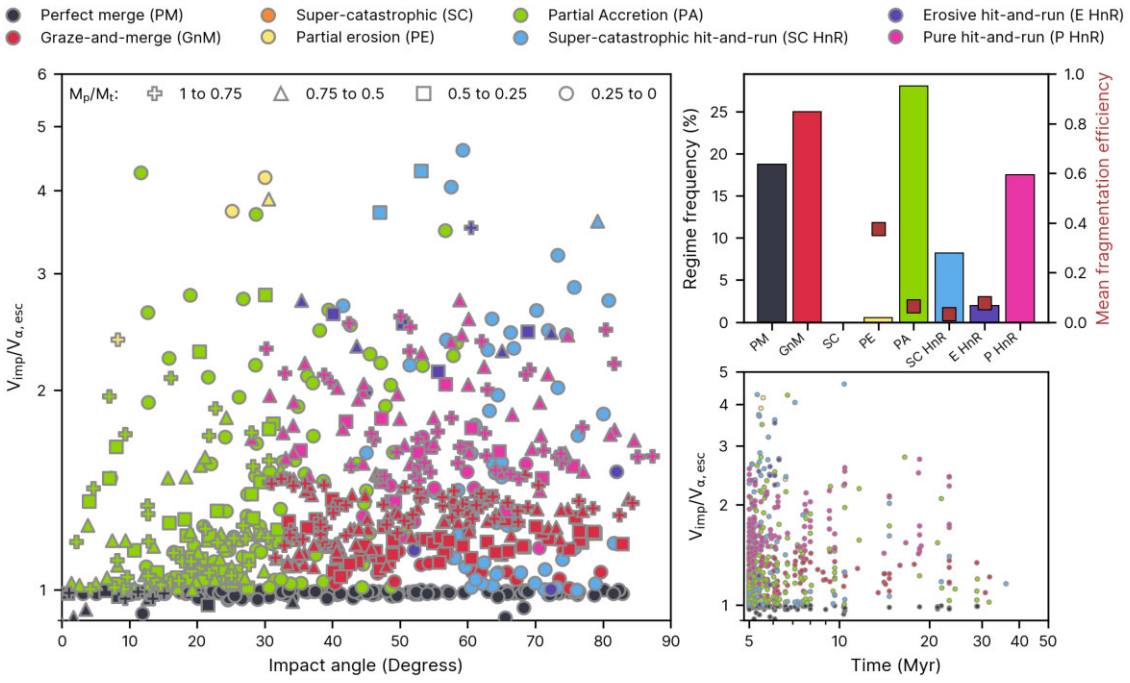

Figure 6. Same as Fig. 4, but for collisions taking place after the gas disc dispersal, from 5 to 50 Myr.

mean fragmentation efficiency of each regime. If we compare the results of Figs 4 and 6 it is evident that collisions after the gas disc dispersal tend to happen at higher impact velocities, which is expected due to the lack gas tidal damping. About 44 per cent of all collisions fall in the perfect merge and graze-and-merge regimes, compared to 43 per cent of the collisions in the gas disc phase. 28 and 17 per cent of the collisions correspond to the partial accretion and pure hit-and-run regimes, respectively. 10 per cent of the collisions fall into the supercatastrophic and erosive hit-and-run regimes. Partial erosion corresponds to only 0.5 per cent of the all collisions taking place after gas dispersal. Except for the collisions in the partial erosion regimes, the fraction of the colliding mass fragmented in non-accretionary events tends to be lower than ∼10 per cent. Collisions in the partial erosion regime fragmented on average 40 per cent of the colliding mass. The right-bottom panel of Fig. 6 shows that most collisions taking place after the gas disc dispersal happen shortly after the gas is gone (first 5 Myr). This is consistent with the results of Izidoro et al. (2017, 2021a). Finally, Fig. 7 shows that imperfect accretion has no dramatic impact on the timing of the last giant impact on super-Earths [see Kokubo & Genda (2010) for a similar conclusion in the context of the Solar system].

Our results show that the BTC scenario typically leads to collisions that result in limited fragmentation. The total mass in fragments produced in typical collisions corresponds to less than 10 per cent of the total mass of the colliding planets. The fragmented mass tends to be rapidly accreted by the more massive remnants of the collision and proves to be inefficient in promoting residual planetesimal-driven migration or efficient damping of orbital inclination and eccentricities of close-in [see Deienno et al. (2019) for a similar conclusion in the Solar system context].

5 DISCUSSION

We have showed that from a statistical point of view the effects of collisional fragmentation have negligible impact on the final dynamical architecture of hot super-Earth systems produced in the BTC scenario. We can now discuss other possible effects of collisional fragmentation.

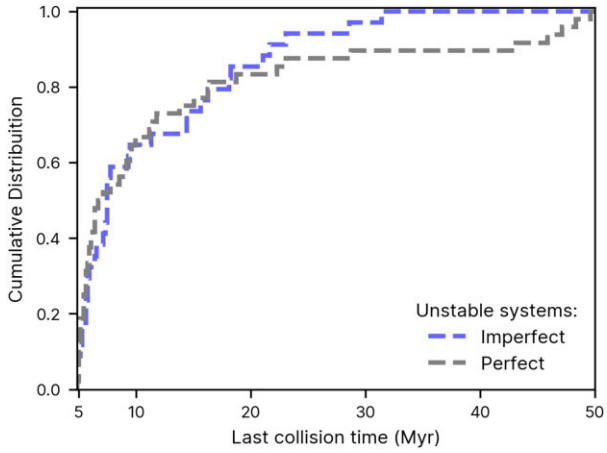

Figure 7. Cumulative distribution of the last collision event taking place after the gas disc phase. We define a giant collision as those involving planetary objects with masses larger than 1 $M_\oplus$ and orbiting within 0.7 au from the star (we have verified that this figure does not change qualitatively when we include all planets with masses $\geq$0.5 $M_\oplus$ and within 2 au). Blue dashed line shows imperfect accretion set simulations, while grey dashed line shows the perfect accretion set simulations.

5.1 Dust production during the instability phase

The presence of dust discs around stars is typically inferred via measurements of infrared excess due to thermal emission of circumstellar dust. Observations suggest that stars older than ∼10 Myr typically do not host hot dust discs (Haisch, Lada & Lada 2001; Wyatt 2008). Although some stars older than ∼10 Myr do show

dust discs, their discs tend to be significantly less massive than discs of much younger stars. This strongly suggests that most stars loose their discs in about 10 Myr. Dust around old discs could be remnants of conventional protoplanetary discs or the result of dust produced via collisions of planets/planetesimals after the dissipation of protoplanetary discs (Wyatt 2008). In this section, we discuss the timing and amount of dust produced in our simulations and discuss our results in the context of disc observations.

Fig. 5 shows that in our model resonant chains tend to become dynamically unstable soon after gas disc dissipation, which lead to orbital crossing and collisions. The instability phase is typically short because of short dynamical time-scales close to the star. Fig. 7 shows that 60 per cent of our systems have their last giant collision within 5 Myr after gas disc dissipation, and 90 per cent of the systems have the last giant collision within 20 Myr. In our simulations, we do not directly model the fate of dust produced in collisions because we truncate the distribution of fragments to a minimal size of 10 Ceres mass. However, we can still estimate the amount of dust that would be produced in our collisions.

Following Leinhardt & Stewart (2012), an erosive collision between two hot super-Earths produces a population of fragments with differential size distribution given by $n(D)\mathrm{d}D \propto D^{-(\beta+1)}\mathrm{d}D$, where $\beta = 2.85$. If we assume that fragments with sizes smaller than 1 m will be converted to dust via collisional cascade, we find that ∼25 per cent of the fragmented mass in our collisions will be converted into dust, where the total mass in fragments typically corresponds to ∼5 per cent of the colliding mass ($M_\mathrm{t} + M_\mathrm{p}$). If two typical super-Earths of 5 $\mathrm{M}_\oplus$ collide in a typical event, the total mass produced in dust grains smaller than <1 m will be about 0.125 $\mathrm{M}_\oplus$. Warm dust has been observed at distances from the star $\lesssim$1 au (e.g. Kennedy & Wyatt 2012; Thompson et al. 2019). Estimates of the dust mass in disc older than 10 Myr yields dust reservoirs of ∼0.01–0.1 $\mathrm{M}_\oplus$ (Wyatt 2008). If for simplicity we neglect dust reaccretion on to the planets, and assume that typical resonant chains exhibit at least a few erosive impacts one can speculate that the BTC scenario would produce an amount of dust that is at least marginally consistent with that observed around stars older than 10 Myr. Dust particles of 1 cm and density of 2 $\mathrm{g\,cm^{-3}}$ at 0.2 au would have a typical lifetime of only 600 kyr, whereas particles at 0.7 au would have a typical lifetime of about 6 Myr (Wyatt & Whipple 1950). The short duration of the instability phase in our simulations together with the expected short lifetime of dust grains in the innermost regions of the disc are also qualitatively aligned with disc observations. Warm dust observed inside 1 au around stars older than ∼100–10 000 Myr (e.g. Thompson et al. 2019) may be (i) the result of late impacts between inner planets subsequent to the BTC; (ii) the result of long-term stable systems becoming eventually unstable; or (iii) collisions of inner planets with leftover outer planetesimals/protoplanets scattered inwards (e.g. Wyatt 2008).

5.2 Mantle-erosive collisions and high bulk density exoplanets

Hot super-Earths are thought to be fully differentiated bodies composed of an iron core, rocky/icy mantle, and a potential thin gaseous envelope. The bulk density of an observed planet may be estimated by combining different observation techniques such as transit, radial velocity, transit timing variations, etc. (e.g. Weiss & Marcy 2014; Hadden & Lithwick 2017). The bulk density of the large majority hot super-Earths remains poorly constrained, but recent studies have suggested that up to ∼20 per cent of the observed innermost hot super-Earths may have bulk densities higher than that of Earth and consistent with that of Mercury (Adibekyan et al. 2021; Schulze et al. 2021). Mercury's mean density is 5.43 $\mathrm{g\,cm^{-3}}$ and it has been proposed to be the outcome of an energetic mantle-stripping collision of two Mars-mass protoplanets (Asphaug & Reufer 2014) during the formation of the terrestrial planets in the Solar system. Mantle-stripping collisions may remove significant part of the planets' mantle potentially leaving behind a high-density iron-rich core (CMF; Marcus et al. 2009; Asphaug & Reufer 2014). In this section, we investigate how common are mantle-stripping collisions in our simulations.

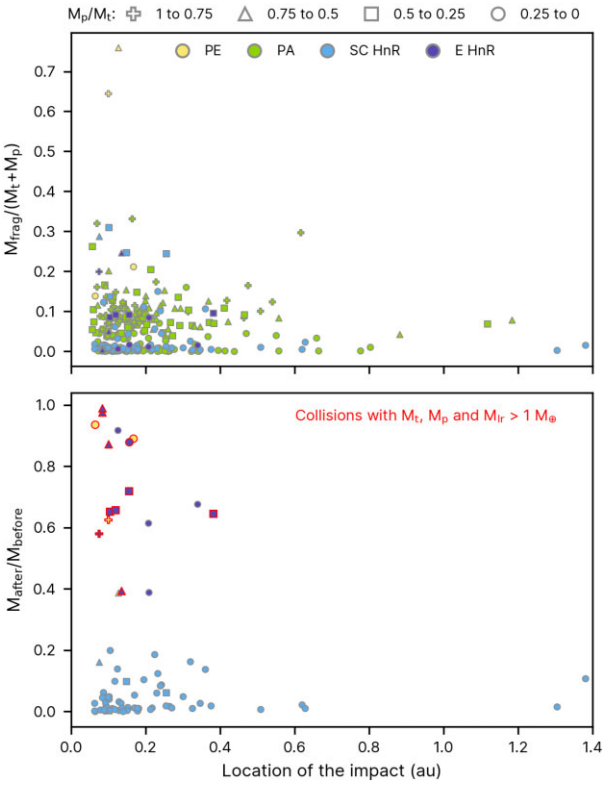

Figure 8. *Top*: Total mass in fragments normalized by the mass of the colliding bodies (M_frag) as a function of the location of the impact. Each data point represents individual collisions taking place after gas disc dissipation. *Bottom*: Remaining mass in erosive collisions as a function of the impact location. Each data point represents one specific eroded planet. In both panels, different symbols are used to represent a given mass ratio interval (top), while the colours represent a specific collisional regime. Collisions highlighted in red are those where the surviving bodies have masses larger than 1 $\mathrm{M}_\oplus$.

We first investigate how the occurrence of imperfect accretion events correlates with the heliocentric distance. The top panel of Fig. 8 shows that the most erosive collisions tend to occur in the innermost regions of the system. Erosive impacts take place inside 0.2 au fragment up to 60–70 per cent of the total colliding mass. Collisions taking place in the innermost regions of the disc tend to be more energetic because of higher orbital velocities in the inner regions of the disc and higher probability of collision with bodies at high-eccentricity orbits. The bottom panel of Fig. 8 shows the mass ratio of planetary bodies experiencing erosive collisions (collisions in the partial accretion regime are not shown) just after and before collision. We do not model the interior structure of planets in this work. Super-Earths are expected to have iron mass fractions varying between ∼10 and 40 per cent and super-Mercuries varying between ∼50 and ∼80 per cent (Adibekyan et al. 2021). We are particularly interested in collisions where from ∼20 to ∼80 per cent of the

putative body mass is eroded during the impact and the remaining body has mass larger than 1 $M_\oplus$. These collisions are the most likely to produce hot super-Earths with high CMF, i.e. super-Mercuries, if a sufficiently large fraction of the mantle is eroded.

We found seven collisions satisfying these criteria, six falling in the erosive hit-and-run regime and one case in the partial erosion regime. We have found that these highly erosive events are noticeably rare and correspond to only 5 per cent of the impacts of bodies more massive than 1 $M_\oplus$. In reality, we have also found that all planetary objects produced in these impacts were subsequently recreated by other more massive planets during the system evolution. Thus, it seems unlikely that the BTC scenario can account for the apparent abundance of super-Earths with high CMF (high densities), the so-called super-Mercuries (e.g. Adibekyan et al. 2021). The iron fraction of some observed inner planets may be higher than the standard picture because inward drifting iron-rich pebbles evaporate and then recondense, increasing the iron fraction of the pebbles close to the iron evaporation front (e.g. Aguichine et al. 2020). This interpretation seems to be aligned with the results of interior models (Dorn et al. 2019) suggesting that in order to account for the composition of a specific set of super-Earths these planets have to form at special locations, where certain elements are less/more abundant in order to explain the planets' peculiar compositions.

6 CONCLUSIONS

In this paper, we have used *N*-body numerical simulations including the effects of planet–disc interaction and pebble accretion to revisit the BTC scenario for the formation of super-Earths (Izidoro et al. 2017, 2021a; Carrera et al. 2019; Lambrechts et al. 2019). Previous simulations of the BTC scenario have modelled collisions as perfect merging events. Here, we compare the results of simulations following this traditional approach with the results of simulations where a more realistic treatment of collisions is considered. We have developed a modified version of the code MERCURY-FLINTSTONE (Chambers 1999; Izidoro et al. 2021a) implementing the algorithm of Leinhardt & Stewart (2012) to resolve collisions, which is calibrated from a suite of impact hydrodynamical simulations. We have performed two sets of 50 simulations starting from the very same initial conditions, with the only difference being the scheme adopted to resolve collisions. In one case, collisions are modelled as perfect merging events conserving mass and linear momentum ('perfect' set). In the other case, collisions are modelled allowing imperfect accretion ('imperfect' set). In our simulations, protoplanetary embryos grow from roughly Moon mass to larger masses by accreting pebbles and collisional fragments in the disc. As planets grow, they migrate inwards reaching the disc inner edge and forming long chains of mean motion resonances. The gas disc is assumed to dissipate at 5 Myr and our simulations are extended in a gas-free scenario up to 50 Myr. After the gas disc dispersal, a large fraction of our compact resonant chains becomes dynamically unstable. We refer to this as the BTC scenario. We have compared the dynamical architecture of planetary systems produced in our two set of simulations at two different epochs, namely at the time of the gas disc dispersal and at the end of our simulations. We compared the period ratio, mutual spacing, orbital eccentricity, orbital inclinations, mass, and planet multiplicity distributions of the perfect and imperfect sets of simulations and found that both approaches lead to statistically equivalent results. This is true when we compare our systems both at the end of the gas disc phase and at 50 Myr, i.e. after the instability phase. Although imperfect accretion events are very common, accounting for more than 50 per cent of the collisions, we found that these collisions typically lead to limited fragmentation. Only ∼10 per cent of the system mass is fragmented during a typical 'late instability phase'. In addition, most fragments are rapidly reaccreted rather than ejected from the system. Although applied in a different scenario, our results are qualitatively aligned to the results of previous studies modelling the formation of terrestrial planets (Kokubo & Genda 2010; Chambers 2013; Walsh & Levison 2016; Clement et al. 2019; Deienno et al. 2019; Walsh & Levison 2019) and super-Earths, including the effects of imperfect accretion (Poon et al. 2020; Scora et al. 2020). Imperfect accretion has negligible effect on the formation and dynamical configuration of hot super-Earth systems. Future studies of the BTC scenario should now focus on the role of giant impacts on sculpting the atmospheric envelopes of hot super-Earths.

ACKNOWLEDGEMENTS

We are very grateful to the referee, John Chambers, for comments and suggestions that helped to improve our paper. LE is grateful to Fundação de Amparo à Pesquisa do Estado de São Paulo (FAPESP) for financial support through grants 19/02936-0, 20/07689-8, and 21/00628-6. AI thanks Conselho Nacional de Desenvolvimento Científico e Tecnológico (CNPq) proc. 313998/2018-3 and FAPESP procs. 16/19556-7 and 16/12686-2 for support during the initial development of this work. AI also thanks NASA for support via grant 80NSSC18K0828 to Rajdeep Dasgupta, during preparation and submission of the work. BB thanks the European Research Council (ERC Starting Grant 757448-PAMDORA) for their financial support. SNR thanks the CNRS's PNP programme for support. OCW thanks (CNPq) proc. 312813/2013-9 and FAPESP proc. 16/24561-0 for financial support. OCW and AI thank the Brazilian Federal Agency for Support and Evaluation of Graduate Education (CAPES) in the scope of the CAPES-Print programme, process number 88887.310463/2018-00, and International Cooperation Project number 3266.

DATA AVAILABILITY

The data underlying this article will be shared on reasonable request to the corresponding author.

REFERENCES

Adibekyan V. et al., 2021, Science, 374, 330
Aguichine A., Mousis O., Devouard B., Ronnet T., 2020, ApJ, 901, 97
Asphaug E., Reufer A., 2014, Nat. Geosci., 7, 564
Benz W., Asphaug E., 1999, Icarus, 142, 5
Bitsch B., Kley W., 2010, A&A, 523, A30
Bitsch B., Kley W., 2011, A&A, 536, A77
Bitsch B., Izidoro A., Johansen A., Raymond S. N., Morbidelli A., Lambrechts M., Jacobson S. A., 2019, A&A, 623, A88
Carrera D., Ford E. B., Izidoro A., 2019, MNRAS, 486, 3874
Chambers J. E., 1999, MNRAS, 304, 793
Chambers J. E., 2013, Icarus, 224, 43
Chatterjee S., Ford E. B., 2015, ApJ, 803, 33
Clement M. S., Kaib N. A., Raymond S. N., Chambers J. E., Walsh K. J., 2019, Icarus, 321, 778
Coleman G. A. L., Nelson R. P., 2014, MNRAS, 445, 479
Cossou C., Raymond S. N., Hersant F., Pierens A., 2014, A&A, 569, A56
Cresswell P., Nelson R. P., 2008, A&A, 482, 677
Deienno R., Walsh K. J., Kretke K. A., Levison H. F., 2019, ApJ, 876, 103
Dorn C., Harrison J. H. D., Bonsor A., Hands T. O., 2019, MNRAS, 484, 712

Duncan M. J., Levison H. F., Lee M. H., 1998, AJ, 116, 2067
Esteves L., Izidoro A., Raymond S. N., Bitsch B., 2020, MNRAS, 497, 2493
Fendyke S. M., Nelson R. P., 2014, MNRAS, 437, 96
Flock M., Turner N. J., Mulders G. D., Hasegawa Y., Nelson R. P., Bitsch B., 2019, A&A, 630, A147
Fressin F. et al., 2013, ApJ, 766, 81
Genda H., Kokubo E., Ida S., 2012, ApJ, 744, 137
Hadden S., Lithwick Y., 2017, AJ, 154, 5
Haisch Karl E. J., Lada E. A., Lada C. J., 2001, AJ, 121, 2065
Hansen B. M. S., 2014, MNRAS, 440, 3545
Howard A. W. et al., 2012, ApJS, 201, 15
Ida S., Lin D. N. C., 2008, ApJ, 685, 584
Ida S., Lin D. N. C., 2010, ApJ, 719, 810
Izidoro A., Ogihara M., Raymond S. N., Morbidelli A., Pierens A., Bitsch B., Cossou C., Hersant F., 2017, MNRAS, 470, 1750
Izidoro A., Bitsch B., Raymond S. N., Johansen A., Morbidelli A., Lambrechts M., Jacobson S. A., 2021a, A&A, 650, A152
Izidoro A., Bitsch B., Dasgupta R., 2021b, ApJ, 915, 62
Johansen A., Lambrechts M., 2017, Annu. Rev. Earth Planet. Sci., 45, 359
Johansen A., Davies M. B., Church R. P., Holmelin V., 2012, ApJ, 758, 39
Kennedy G. M., Wyatt M. C., 2012, MNRAS, 426, 91
Kokubo E., Genda H., 2010, ApJ, 714, L21
Lambrechts M., Morbidelli A., Jacobson S. A., Johansen A., Bitsch B., Izidoro A., Raymond S. N., 2019, A&A, 627, A83
Lee E. J., Chiang E., Ormel C. W., 2014, ApJ, 797, 95
Leinhardt Z. M., Stewart S. T., 2012, ApJ, 745, 79
Levison H. F., Duncan M. J., Thommes E., 2012, AJ, 144, 119
Levison H. F., Kretke K. A., Duncan M. J., 2015, Nature, 524, 322
McNeil D. S., Nelson R. P., 2010, MNRAS, 401, 1691
Marcus R. A., Stewart S. T., Sasselov D., Hernquist L., 2009, ApJ, 700, L118
Marcy G. W., Weiss L. M., Petigura E. A., Isaacson H., Howard A. W., Buchhave L. A., 2014, Proc. Natl. Acad. Sci. USA, 111, 12655
Masset F. S., Morbidelli A., Crida A., Ferreira J., 2006, ApJ, 642, 478
Mayor M. et al., 2011, preprint (arXiv:1109.2497)
Morbidelli A., Bottke W. F., Nesvorný D., Levison H. F., 2009, Icarus, 204, 558
Mulders G. D., Pascucci I., Apai D., Ciesla F. J., 2018, AJ, 156, 24
Ogihara M., Ida S., 2009, ApJ, 699, 824
Ogihara M., Morbidelli A., Guillot T., 2015, A&A, 578, A36
Ogihara M., Kokubo E., Suzuki T. K., Morbidelli A., 2018, A&A, 615, A63
Petigura E. A., Marcy G. W., Howard A. W., 2013, ApJ, 770, 69
Poon S. T. S., Nelson R. P., Jacobson S. A., Morbidelli A., 2020, MNRAS, 491, 5595
Raymond S. N., Barnes R., Mandell A. M., 2008, MNRAS, 384, 663
Romanova M. M., Lovelace R. V. E., 2006, ApJ, 645, L73
Schulze J. G., Wang J., Johnson J. A., Gaudi B. S., Unterborn C. T., Panero W. R., 2021, Planet. Sci. J., 2, 113
Scora J., Valencia D., Morbidelli A., Jacobson S., 2020, MNRAS, 493, 4910
Stewart S. T., Leinhardt Z. M., 2012, ApJ, 751, 32
Terquem C., Papaloizou J. C. B., 2007, ApJ, 654, 1110
Thompson M. A., Weinberger A. J., Keller L. D., Arnold J. A., Stark C. C., 2019, ApJ, 875, 45
Volk K., Gladman B., 2015, ApJ, 806, L26
Wallace J., Tremaine S., Chambers J., 2017, AJ, 154, 175
Walsh K. J., Levison H. F., 2016, AJ, 152, 68
Walsh K. J., Levison H. F., 2019, Icarus, 329, 88
Weiss L. M., Marcy G. W., 2014, ApJ, 783, L6
Wyatt M. C., 2008, ARA&A, 46, 339
Wyatt S. P., Whipple F. L., 1950, ApJ, 111, 134

This paper has been typeset from a TEX/LATEX file prepared by the author.